Research Article

Nano Research
2022, 15(6): 5678–5686

ISSN 1998-0124 CN 11-5974/O4
https://doi.org/10.1007/s12274-022-4139-3

Mechanically durable, super-repellent 3D printed microcell/nanoparticle surfaces

Sajad Haghanifar[1], Anthony J Galante[1], Mehdi Zarei[2], Jun Chen[3], Susheng Tan[3], and Paul W Leu[1,2,4] (✉)

[1] *Department of Industrial Engineering, University of Pittsburgh, Pittsburgh, PA 15261, USA*
[2] *Department of Mechanical Engineering and Materials Science, University of Pittsburgh, Pittsburgh, PA 15261, USA*
[3] *Department of Electrical and Computer Engineering and Peterson Institute of NanoScience and Engineering, University of Pittsburgh, Pittsburgh, PA 15261, USA*
[4] *Department of Chemical Engineering, University of Pittsburgh, Pittsburgh, PA 15261, USA*

Received: 6 October 2021 / **Revised:** 13 December 2021 / **Accepted:** 4 January 2022

ABSTRACT

Three-dimensional (3D) printed re-entrant micropillars have demonstrated high static contact angles for an unprecedented variety of liquids, but have yet to achieve this with low contact angle hysteresis and excellent abrasion resistance. We report on the demonstration of 3D printed microcell/nanoparticle structures that exhibit high static contact angle, low contact angle hysteresis, and high mechanical durability. Micropillars and microcells both exhibit high static contact angles with water and ethylene glycol (EG), but suffer from high contact angle hysteresis, indicative of rose petal wetting. Our modeling results indicate that micropillars are able to achieve higher static contact angle and breakthrough pressure simultaneously compared with microcells. However, simulations also indicate that micropillars have higher maximum equivalent stress at their bases, so that they are more prone to mechanical failure. We address contact angle hysteresis and mechanical durability issues by the creation of 3D printed microcell/nanoparticle arrays that demonstrate super-repellency and retain their super-repellency after 100 cycles of mechanical abrasion with a Scotch-Brite abrasive pad under a pressure of 1.2 kPa. The use of interconnected microcell structures as opposed to micropillars addresses mechanical durability issues. Low contact angle hysteresis is realized by coating 3D printed structures with low surface energy nanoparticles, which lowers the solid–liquid contact area fraction. Our results demonstrate new 3D printed structures with mechanical durability and super-repellency through the use of microcell structures integrated with fluorinated nanoparticles.

KEYWORDS

superomniphobicity, three-dimensional (3D) printing, surface evolver, mechanical durability, microcell, re-entrant, micropillar

1 Introduction

Super-repellent surfaces are desirable for a wide variety of functionalities such as self-cleaning [1–3], condensation resistance (or anti fogging) [4–6], stain resistance [7], anti-icing [8, 9], anti-biofouling [10], and anti-virofouling [11]. Applications are wide-ranging including for optoelectronics [12], textiles, healthcare, and household use [13]. Super-repellent surfaces are defined by high static contact angle > 150° and small contact angle hysteresis < 10° for not only water, but also various oils with low surface tension [14–18]. These surfaces achieve high static contact angles through Cassie–Baxter wetting [19], where the fraction of contact area between the solid and liquid must be very small [20, 21]. Common strategies for creating surfaces with high water static contact angle have included a combination of hierarchical micro-/nanostructures and hydrocarbon/fluorocarbon compounds [4, 7]. Surfaces with high water static contact angle have been widely demonstrated in the literature due to water's relatively high surface tension of 72.8 mN/m.

In contrast, creating surfaces with high oil contact angle is significantly more challenging. This is because the surface tensions of oils and other organic liquids are lower than water, and thus they tend to spontaneously spread across surfaces and past trapped air [22–24]. Recent theoretical work has suggested that the key to achieving high static contact angle for a variety of liquids is the use of re-entrant structures [14, 16–18]. Re-entrant micro-/ nanostructured surfaces create a more robust metastable solid–liquid–air interface consistent with Cassie–Baxter wetting such that they are able to repel liquids other than simply water.

One versatile method capable of creating complex re-entrant structures is three-dimensional (3D) printing via direct laser writing using a non-linear two-photon polymerization process [25–29], as well as transfer printing [30]. A variety of re-entrant geometry structures have been demonstrated via 3D printing including springtail-inspired triply re-entrant micropillars [25, 28], *Salvinia molesta* leaf-inspired eggbeater head microhairs [26], and bi-Gaussian stratified plateau-inspired re-entrant micropillars [27]. These structures have demonstrated unprecedented static contact angles with different liquids, but are not truly super-repellent as they tend to suffer from high contact angle hysteresis (and high rolling angle).

Address correspondence to pleu@pitt.edu

Creating re-entrant structures with high static contact angle along with low contact angle hysteresis indicative of super-repellency for a variety of liquids has yet to be demonstrated by 3D printing. Lie et al. reported on the 3D printed triply re-entrant micropillar arrays with a contact angle of > 150° for water and various oils, but the hysteresis value reported for water was approximately 20° for a pitch of 80 μm and top diameter of 30 μm [25]. The structures exhibit higher hysteresis values up to 40° for oil [25]. Stratified re-entrant micropillars similarly demonstrate a water static contact angle of 156.4°, but a high contact angle hysteresis of 53.1° [27]. When a surface exhibits high static contact angle, but also high contact angle hysteresis, this type of wetting is known as rose petal wetting [31, 32], where droplets remain adhered to the surface when tilted. The high contact angle hysteresis is indicative of strong adhesion between the surfaces and the surface can sometimes even be tilted upside down while the droplet remains adhered [33]. Rose petal wetting has also been referred to as parahydrophobicity in the Refs. [33, 34]. This is in contrast with lotus leaf wetting where the surface exhibits both high water static contact angle (> 150°) as well as low surface contact angle hysteresis (< 10°), which is indicative of low adhesion between the surface and the droplet [10, 35, 36]. In lotus leaf wetting, water droplets easily roll off the surface, with even the slightest tilt. Super-repellency requires lotus leaf wetting not only with water, but also other low surface tension liquids.

An additional major challenge in creating super-repellent surfaces is that they typically have limited robustness against mechanical abrasion [37]. Surfaces with high static contact angles utilize microscale or nanoscale roughness to create very small fraction of contact area between the solid and liquid, but these surfaces experience high local mechanical stresses such that they easily abrade away [38]. Structures with self-similarity [11, 39] or self-healing [4, 40] are some strategies for addressing this issue. The self-similarity approach has been demonstrated in 3D printed structures by printing stratified re-entrant micropillars of different heights [27]. These structures retain their high static contact angle after frictional abrasion. However, these structures have high contact angle hysteresis as discussed above (53.1° with water) and the frictional abrasion assessed consisted of only a triangular rubber wiper with a normal load of 0.2 N. This represents a very mild frictional abrasion condition. 3D printed surfaces thus far have focused on micropillar-like structures, which have limited mechanical reliability against abrasion due to their protrusive topography.

In this paper, we report on the demonstration of mechanically robust super-repellent microcell/nanoparticle structures that exhibit high static contact angles with water and organic liquids as well as ultra-low contact angle hysteresis and excellent abrasion resistance. Our modeling shows the tradeoffs between static contact angle and breakthrough pressure that exist in creating these structures. Structures with high static contact angles tend to have low breakthrough pressures and vice versa.

The modeling demonstrates that in principle, micropillar arrays may achieve higher static angle and breakthrough pressure simultaneously compared with microcell arrays. Triply-reentrant structures as well as dual-leveled structures provide for multiple metastable wetting states with different failure mechanisms, where the redundancy provided from the different local energy minima provides for better stability of Cassie–Baxter wetting. Static structural finite element simulations indicate that the micropillars have over 3 times greater equivalent stress than the microcell structures and this maximum stress occurs at the base of the structure as opposed as to the top. The modeling work suggests that while micropillars can achieve higher static contact angle and breakthrough pressure simultaneously compared with microcells, they are less mechanically durable.

Both fabricated re-entrant micropillars and microcells demonstrate high static contact angles with water and ethylene glycol (EG), but also high contact angle hysteresis (> 30°). Coating the micropillars and microcells with fluorinated SiO_2 nanoparticles addresses contact angle hysteresis issues. The micropillar/nanoparticle structures exhibit high static contact angles with water and ethylene glycol of 170.0° ± 1.5° and 161.0° ± 2.5°, respectively, and low contact angle hysteresis values of 2.0° ± 1.5° and 4.5° ± 2.0°, respectively. However, the re-entrant pillar arrays are easily destroyed after just the very first cycle of abrasion. The mechanical durability of 3D printed, superomniphobic structures is improved with interconnected microcells as opposed to micropillars. Our re-entrant microcell/nanoparticle structures exhibit static contact angles for water and ethylene glycol oil of 167.3° ± 1.8° and 159.5° ± 2.5°, respectively. The contact angle hysteresis values for water and ethylene glycol were 2.5° ± 1.5° and 4.5° ± 2.0°, respectively. After 100 cycles of abrasion with a Scotch-Brite abrasive pad under a pressure of 1.2 kPa, the microcells exhibit static contact angles of 152.0° ± 3.5° and 145.0° ± 5.5°, for water and ethylene glycol, respectively, with hysteresis of 7.1° ± 2.5° and 13.0° ± 6.5°, respectively.

Our results demonstrate new 3D printed structures with mechanical durability and super-repellency through the use of microcell structures integrated with fluorinated nanoparticles. The fabricated re-entrant microcell array can find potential applications in various industries including but not limited to electronic devices, medical devices, and optoelectronics.

2 Experimental and simulation methods

2.1 3D printing

The microstructures described were 3D printed by two-photon absorption polymerization (Photonic Professional GT, Nanoscribe GmbH) over a 4 mm × 4 mm area. Polished Si wafers (thickness = 500 μm) were used as substrates. The substrates were cleaned by ultrasonic rinse in acetone (C_3H_6O), isopropanol (IPA) and distilled water for 5 min each, and then dried by N_2. Negative photoresist IP-S (Nanoscribe GmbH) with a refractive index of 1.48 at 780 nm was used in the Dip-in Laser Lithography (DiLL) configuration. The laser power and scan speed were set at 50 mW and 30 mm/s, respectively. After printing, the samples were developed in SU-8 developer for 20 min followed by rinsing in IPA for 5 min. Finally, the samples were dried by gently blowing with N_2. To increase the adhesion of the walls to the Si surface, a film (10 μm thick) of the resist was first printed on the Si substrate before the microstructures were printed on the resist film.

2.2 Nanoparticle coating method

SiO_2 nanoparticles were coated onto the microstructures followed by drying on a hot plate at 100 °C for 30 min. The preparation of the nanoparticle solution was as follows: 5 mL of tetraethyl orthosilicate (TEOS), 250 μL of perfluorinated compound, and heptadecafluorotrimethoxysilane (HFAS), were dissolved in 25 mL ethanol (C_2H_5OH). The solution was mixed with ammonium hydroxide/ethanol solution (6 mL 28% NH_3:H_2O in 25 mL ethanol), and stirred at room temperature for 12 h [41]. The solution was then ultrasonicated (VCX750 Sonics & Materials Inc.) for 30 min to produce a homogeneous suspension prior to the coating onto substrates [41]. Upon drying at room temperature, the treated substrate was further cured at 110 °C for 1 h.

2.3 Wetting simulations

The wetting properties of the structures were simulated using Surface Evolver [42] to evaluate the effect of the location of the liquid–solid–vapor three-phase contact line on (1) the static contact angle θ_{CB} and (2) the breakthrough pressure P_B. The droplet was given the surface tension of water (72.8 mN/m). The water droplet was constrained to be constant volume and total energy was minimized in the simulation. Gravity was included as well in the simulations. A 3 × 3 array was utilized for the micropillars and a hexagon consisting of 6 microcells were used for the simulations.

2.4 Mechanical properties simulations

In order to evaluate mechanical properties of designed structures, the two structures were simulated using static structural finite element analysis with Ansys. The 3D printed photoresist IP-S is homogenous and isotropic with a Young's modulus of 2.6 GPa and Poisson's ratio of 0.4 [43]. A downward pressure of 1.2 kPa was applied at the top plane and a coefficient of friction of 0.7 was assumed for Scotch-Brite pad [44]. The bottom planes for both structures were fixed. Periodic boundary conditions were used for the microcell structures. Convergence analysis was performed on the structures so that the change in maximum equivalent stress was less than 3%.

2.5 Breakthrough pressure experiments

Breakthrough pressure experiments were additionally performed on the structures by observing a single water droplet evaporates on the samples. A 5 μL drop of water was placed on each substrate and evaporated while monitoring the decrease of the contact angle [7]. This experiment was repeated 3 times per sample. The breakthrough pressure was calculated based on estimates of the contact line radius at breakthrough transition determined from fits of the droplet shape by the goniometer.

2.6 Abrasion experiments

A Taber Linear Abraser (model 5750) with weighted Scotch-Brite abrasive pad was used for abrasion of the samples on a constant surface area of 4×10^{-4} m^2. A pressure of 1.2 kPa was applied.

3 Results and discussion

Figure 1 shows schematics of the structures fabricated. The cross-section of the structures consists of triply re-entrant shapes (Fig. 1(a)), which are used to enhance the liquid repellency. Liu et al. demonstrated that dual-level re-entrant geometry, meaning re-entrant geometry at the top of the pillar and at the middle of the height of the pillar can improve the repellency for lower surface tension liquids [25]. Therefore we utilized a dual-level re-entrant cross-section for both the micropillars and microcells. The unit cell, top view and tilted view of the micropillars and microcells arrays are also shown in Fig. 1(b). The micropillars consist of rotating the cross section around a center axis, and the micropillars are placed in a square array. The microcells consist of the cross section geometry translated along lines in a triangular array.

Structures with large static contact angles are typically created through surfaces with small liquid–solid contact fraction, f_s. This is because in the ideal Cassie–Baxter wetting state

$$\cos\theta_{CB} = f_s\cos\theta_Y - f_g = f_s(\cos\theta_Y + 1) - 1 \quad (1)$$

where θ_{CB} is the apparent contact angle in the Cassie–Baxter state and θ_Y is the intrinsic Young's contact angle of the liquid on the surface. As can be seen from this equation, a small f_s is desirable for a large apparent contact angle, θ_{CB}. The solid fraction for the micropillar geometry can be calculated as

$$f_{s,p} = \frac{\pi D^2}{4P^2} \quad (2)$$

where D is the diameter of the re-entrant top and P is the pitch. For the microcell array, the solid fraction is

$$f_{s,c} = \frac{W(2P - W)}{P^2} \quad (3)$$

where W is the width of the re-entrant top and P is the pitch.

In addition to the apparent contact angle, the breakthrough pressure is another important design parameter. The breakthrough pressure determines the thermodynamic stability of droplets in the Cassie–Baxter state. The breakthrough pressure is the Laplace pressure at which the droplet transitions from the local energy minimum in the Cassie–Baxter state into the Wenzel state. The breakthrough pressure can be calculated from the ratio of the unit maximum surface energy to the unit stress area [45]. For micropillar arrays, the breakthrough pressure is

$$P_{b,p} = \frac{4\pi D}{4P^2 - \pi D^2}\gamma \quad (4)$$

where γ is liquid surface energy [25]. For the microcells, the breakthrough pressure is

$$P_{b,c} = \frac{4}{P - W}\gamma. \quad (5)$$

Figure 2 shows the wetting behavior of micropillar arrays of different diameter and pitch (Fig. 2(a)) and microcell arrays of various width and pitch (Fig. 2(b)). The Figs. 2(a)(i) and 2(b)(i) apparent contact angle θ_{CB} and Figs. 2(a)(ii) and 2(b)(ii) breakthrough pressure P_b shown are based on Eqs. (1)–(5). We assume the smallest possible micropillars have a diameter of D = 5 μm and microcells have the smallest width of W = 5 μm based on 3D printing resolution. In principle, structures as small

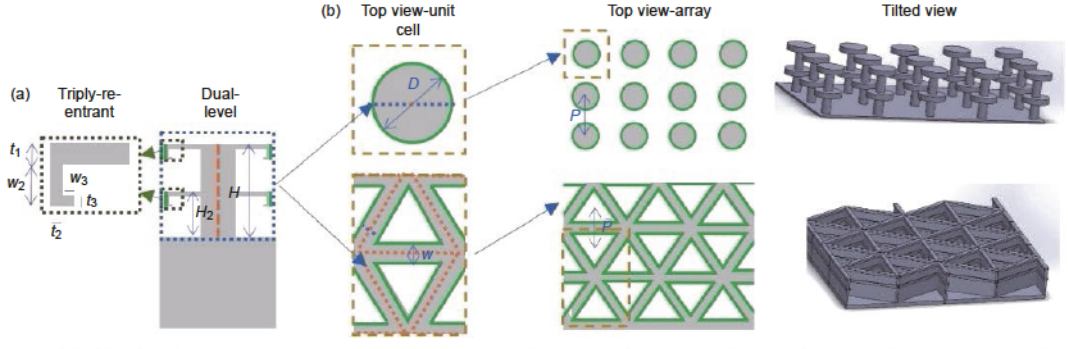

Figure 1 Schematic of dual-level triply re-entrant (a) cross section for (b) micropillar array and (c) microcell array. The micropillar array consists of rotating the cross-section around a center axis while the microcell array consists of translating the cross-section into a triangular lattice.

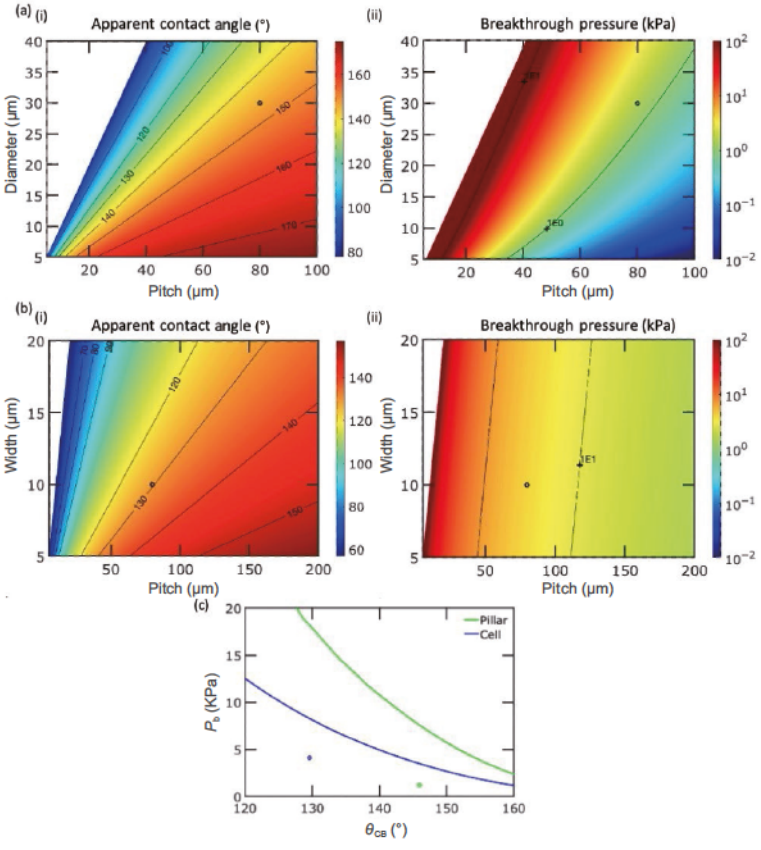

Figure 2 Static wetting properties of (a) micropillar and (b) microcell arrays. (i) Apparent contact angle θ_{CB} and (ii) breakthrough pressure P_b for various widths and pitches. The fabricated micropillar and microcell array is marked in the figures with a black circle. P_b is plotted on a log-scale. (c) Pareto frontier of θ_{CB} and P_b achievable for micropillars with a minimum diameter of 5 μm and microcells with a minimum width of 5 μm. The fabricated micropillars and microcells are shown with circles.

as 1 μm diameter and width can be printed, though there may be issues with imprecision and imperfections and the time needed to create such small structures over larger areas. The contour plots show all values of breakthrough pressure greater than 10^3 kPa for the micropillars and greater than 10^4 kPa for the microcells at those values. As can be seen from Figs. 2(a) and 2(b), there is a tradeoff between achieving high apparent contact angles and high breakthrough pressure. Structures with larger pitches tend to have smaller solid fractions and thus, higher apparent contact angles. However, larger pitches result in smaller breakthrough pressures and thus, the Cassie–Baxter wetting state is less stable. Figure 2(c) plots the Pareto frontier of the apparent contact angle and breakthrough pressure achievable assuming a minimum micropillar diameter D = 5 μm and microcell width W = 5 μm. Micropillars are capable of achieving higher apparent contact angle and breakthrough pressure simultaneously than microcells.

In order to be able to create structures with both large apparent contact angles and breakthrough pressures, it is necessary to create pillars with diameter as small as possible or cells with width as small as possible. Methods such as reactive ion etching and chemical vapor deposition have been utilized to create pillar-like structures at the nanoscale [4, 46–48] and nanoscale cavities or holes [49]. Re-entrant nanopillars have been demonstrated with high apparent contact angles for a wide variety of liquids and high breakthrough pressures [4, 7]. For example, glasswing butterfly inspired surfaces demonstrated static water and ethylene glycol contact angles of 162.1° ± 2.8° and 155.2° ± 2.28°, respectively, with an approximate breakthrough pressure of 30 kPa [4]. Re-entrant nanocavities have also been created for anti-fogging [5]. However, these nanomanufacturing methods lack the tunable control of 3D printing described here and are only able to achieve singly re-entrant structures.

Micropillars and microcells that balance the tradeoff between apparent contact angle and breakthrough pressure were simulated in more detail and fabricated. The micropillars have a diameter D = 5 μm and pitch P = 80 μm, while the microcells have a width W = 10 μm, and pitch P = 80 μm. According to the analytical equations above, for micropillars, the apparent contact angle $\theta_{CB,p}$ = 146.0° and the breakthrough pressure $P_{b,p}$ = 1.20 kPa. For the microcells, the apparent contact angle $\theta_{CB,c}$ = 129.6° and the breakthrough pressure $P_{b,c}$ = 4.13 kPa. The theoretical apparent contact angles and breakthrough pressures of the fabricated micropillars and microcells are shown in Fig. 2 with circles.

Figure 3 shows the detailed simulation results. For both the micropillars and microcells, the rest of the geometry based on the schematic shown in Fig. 1 is defined by H = 50 μm, H_2 = 25 μm, t_1 = 2 μm, t_2 = 1 μm, t_3 = 1 μm, W_2 = 4 μm, and W_3 = 1 μm. The micropillar dimensions are the same as those in Liu et al. [25], which was determined to be optimal for achieving high apparent static contact angle with micropillars.

The liquid droplet was found to pin in three different metastable locations on the triply reentrant cross-section of the micropillars or microcells (Fig. 3(a)). Figure 3(b) shows the simulation results at different three-phase contact line pinning locations for the water droplet. The results agree fairly well with that of the analytical equations where the droplets are assumed to pin at location 1. The static contact angles and breakthrough pressures are the highest when the droplet is pinned at location 2 on the structures. Figure 3(c) shows the equilibrium shape of the droplet where the three-phase contact line is pinned at location 2 on the structures and the static contact angles are $\theta_{CB,p}$ = 151.0° and $\theta_{CB,c}$ = 141.0°. Figure 3(d) displays snapshots of breakthrough pressure simulation when the droplet contact line is pinned at location 2. In our simulations, two different transition modes were

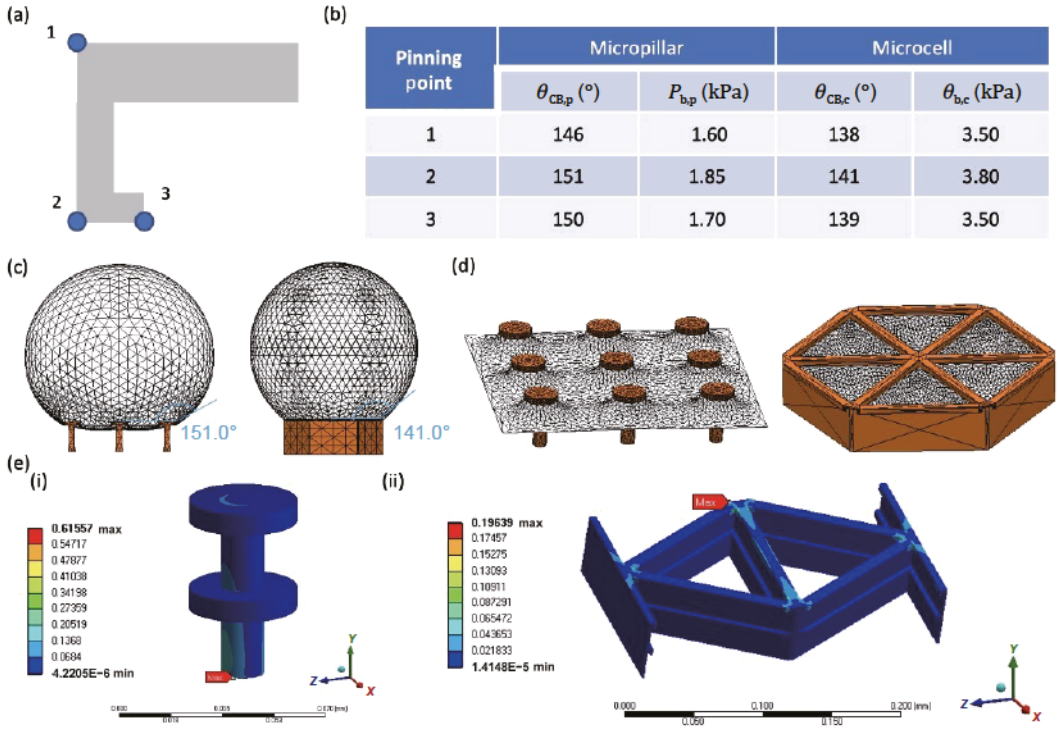

Pinning point	Micropillar		Microcell	
	$\theta_{CB,p}$ (°)	$P_{b,p}$ (kPa)	$\theta_{CB,c}$ (°)	$\theta_{b,c}$ (kPa)
1	146	1.60	138	3.50
2	151	1.85	141	3.80
3	150	1.70	139	3.50

Figure 3 Simulation results. (a) Schematic showing three locations where the water may be pinned. (b) Static contact angle θ_{CB} and breakthrough pressure P_b for different contact line pinning locations. Snapshots showing (c) the static contact angle and (d) the breakthrough pressure simulations. (e) Static structural finite element simulation results showing equivalent stress in MPa under 1.2 kPa normal compressive pressure at the top surface and tangential force corresponding to a coefficient of friction of $\mu = 0.7$ for (i) micropillar and (ii) microcell.

observed when the surface can no longer support the curvature of the liquid–air interface and the contact line. For pinning location 1, the droplet was observed to depin on the surface and the droplet continues sliding along the walls of the re-entrant structure. At pinning locations 2 and 3, the droplet bulges and contacts the central pillar or wall in the cross section. Base failure is also possible in these types of structures where the droplet droops and touches the bottom surface [50], though our structures were sufficiently high where this transition mechanism was not observed. These simulations suggest that at least in principle, doubly re-entrant structures should perform as well as triply re-entrant structures since the droplet pinned at location 3, in fact, has a lower static contact angle and breakthrough pressure than the droplet pinned at location 2. There may be advantages to printing triply re-entrant structures in practice though due to printing imprecision and imperfections such as surface roughness. The dual-level printed structures also add another layer of redundancy or self-similarity to the structures which may provide for better stability of Cassie–Baxter wetting in spite of manufacturing defects and imperfections.

Figure 3(e) shows the results of static structural finite element simulations performed on micropillars (Fig. 3(e)(i)) and microcell structures(Fig. 3(e)(ii)). The IP-S photoresist was assumed to have a Young's modulus of E = 2.6 GPa and Poisson's ratio ν = 0.4. Periodic boundary conditions are implemented in the case of the microcavity to capture the semi-infinite nature of the surface. A compressive pressure of 1.2 kPa was applied just like in the experiments and a tangential force corresponding to a sliding coefficient of friction μ = 0.7 was also applied to the surface. The maximum equivalent stresses for the micropillars and microcells are 0.61 and 0.19 MPa, respectively. The micropillars resemble cantilevered beams and the maximum stress occurs near the base of the pillars (as they do in cantilevered beams) where the bending moment is maximum. In contrast, the microcells are interconnected and more truss-like. The maximum equivalent stress occurs at the corners of the triangular holes near the top of the microcell. The equivalent stress for the micropillars is not only over 3 times larger than that of the microcells, but also is in a location, which is more likely to lead to overall failure of the structure. While micropillars may in principle, achieve higher static contact angle and breakthrough pressure simultaneously compared with microcells, they have the key shortcoming of poor mechanical stability as will be confirmed experimentally later.

Figure 4 shows the fabricated micropillars (Fig. 4(a)) and microcells and their wetting properties (Fig. 4(b)). Scanning electron microscopy (SEM) images from the top (Figs. 4(a)(i) and 4(b)(i)) and 15° tilted view (Figs. 4(a)(ii) and 4(b)(ii)) are both shown. For wetting experiments, droplets with 5 μL of volume were used and the measurements were repeated 3 times per sample. Representative liquid droplet images of the wetting behavior of the various substrates are also shown, depicting the high apparent static contact angle (Figs. 4(a)(iii) and 4(b)(iii)) and high contact angle hysteresis (Figs. 4(a)(iv) and 4(b)(iv)) with water. The pillar array before coating shows high apparent static contact angles > 150° for both water (72.8 mN/m) and ethylene glycol (47.7 mN/m). The static contact angles are 156.7° ± 2.1° and 148.5° ± 2.0° for water and ethylene glycol, respectively. However the contact angle hysteresis values for those liquids on these surfaces are large. The contact angle hystereses are 30.0° ± 3.5° and 58.0° ± 10.0° for water and ethylene glycol, respectively. The apparent contact angles for the microcell array are 147.0° ± 2.0° for water and 138.0° ± 2.5° for ethylene glycol. The hysteresis values are also high with 53.0° ± 4.5° and 85.0° ± 6.5° for water and ethylene glycol, respectively. For comparison, the wetting behavior of a flat photoresist (IP-S) surface was also characterized. The apparent water contact angle is 56.8° ± 3.7° and water contact angle hysteresis is 40.2° ± 4.4° (Figs. 4(c)(i) and 4(c)(ii)). The apparent ethylene glycol contact angle is 41.9° ± 4.3° and contact angle hysteresis is 53.1° ± 5.1°. The high contact angle hysteresis values are indicative of rose petal wetting, instead of lotus leaf wetting. Instead of rolling off the surface easily, the droplets remain adhered to the surface even when tilted to large angles.

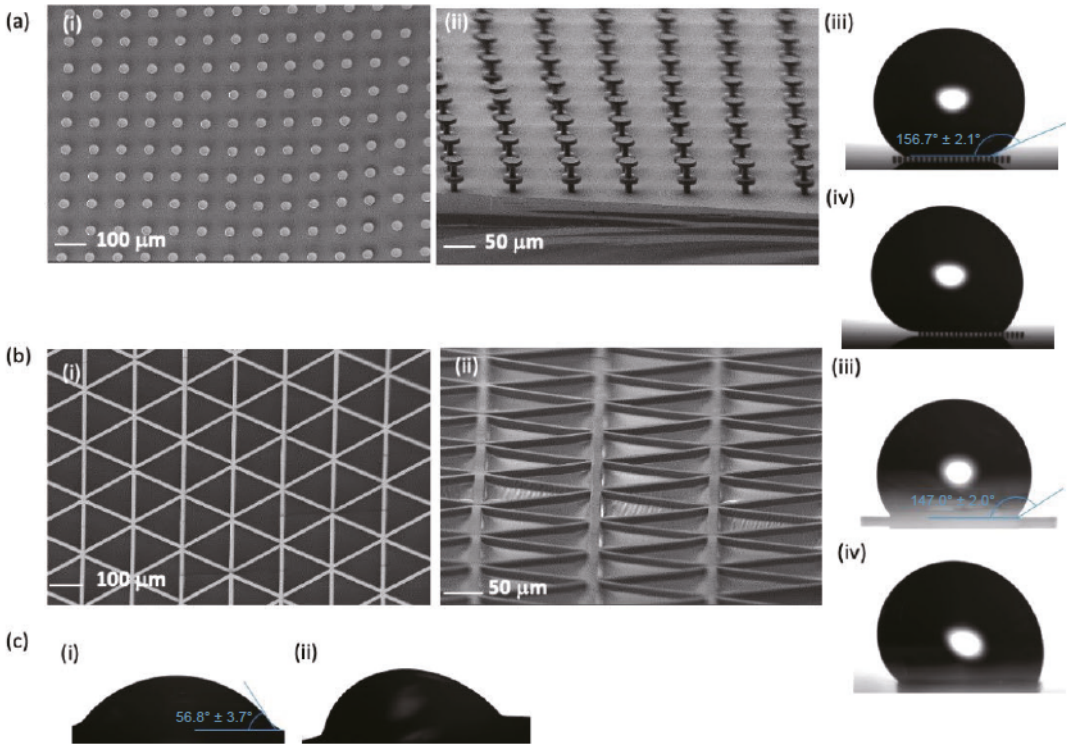

Figure 4 Microstructure and wetting properties of 3D printed microstructures. (a) Micropillar and (b) microcell (i) overhead SEM image, (ii) 15° tilted side view SEM image, (iii) apparent static contact angle, and (iv) tilted image showing high contact angle hysteresis. The water contact angle hysteresis is 30.0° ± 3.5° and 53.0° ± 4.5° for the micropillars and microcells, respectively. (c) Flat sample (i) apparent static contact angle and (ii) tilted image before sliding. The contact angle hysteresis is 40.2° ± 4.4°.

These surfaces are not super-repellent. In addition, the micropillar array samples have a measured breakthrough pressure of 1,020 ± 70 Pa, while the microcell structures have breakthrough pressure of 550 ± 70 Pa.

To reduce contact angle hysteresis, we coated the microstructures with oleophobic, fluorinated SiO_2 nanoparticles. Figure 5 shows the results with the nanoaparticle coating. Contact angle hysteresis may be reduced by reducing the contact area fraction [50] and nanoparticles also have re-entrant geometry. Figure 5(a) shows transmission electron microscopy (TEM) images of the fluorinated SiO_2 nanoparticles. The diameter of the nanoparticles is 39.3 ± 8.1 nm, as calculated using ImageJ software from 5 sample TEM images with an overall count of 247 nanoparticles. Figure 5(b) shows the wetting results of the fluorinated SiO_2 nanoparticles on flat photoresist. The apparent water contact angle is 139.2° ± 5.3° and water contact angle hysteresis is 53.5° ± 4.5°. The apparent ethylene glycol contact angle is 131.8° ± 4.4° and contact angle hysteresis is 65.3° ± 4.8°. The nanoparticles alone do not have super-repellency properties.

Nanosphere lithography methods [51, 52] were utilized to coat the nanoparticles onto the 3D printed structures. The nanoparticles do not coat the surface uniformly due to the 3D morphology of the surface and after drying, the nanoparticles appear clustered on the microstructures. Larger diameter

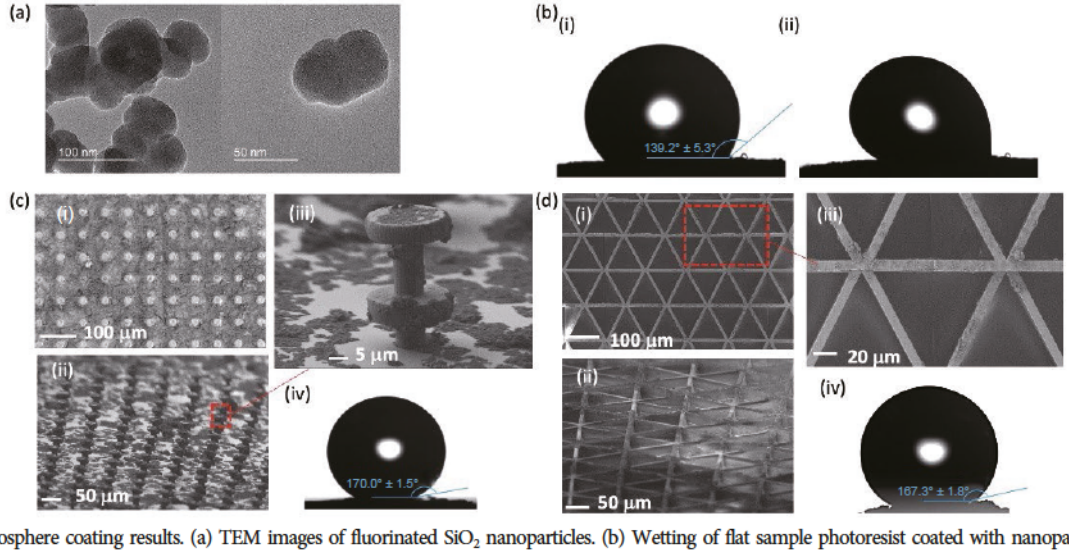

Figure 5 Nanosphere coating results. (a) TEM images of fluorinated SiO_2 nanoparticles. (b) Wetting of flat sample photoresist coated with nanoparticles. (i) Static contact angle and (ii) 15° tilted image. The contact angle hysteresis is 23.3° ± 4.1°. Microstructure and wetting properties of 3D printed samples coated with nanospheres for (c) micropillar and (d) microcell. (i) overhead SEM image and (ii) 15° tilted side view, (iii) zoomed in SEM image, and (iv) apparent water static contact angle image. The contact angle hysteresis of the micropillars with nanospheres and microcells with nanospheres are 1.5° ± 0.5° and 2.5° ± 1.5°, respectively, and too low to be observed.

(≈ 250 nm) polytetrafluoroethylene (PTFE) nanoparticles were also tested but led to worse performance as they may compromise the re-entrant geometry of the micro-pillars. Instead, the smaller diameter (≈ 40 nm) SiO_2 fluorinated nanoparticles were used which create nano-reentrant clusters upon drying, as seen in Fig. 5(a). The oleophobic nanoparticles increase the hierarchical re-entrant roughness (adding both micro-reentrant and nano-reentrant roughness) which improves the static contact angles, hysteresis angles, and breakthrough pressures. The wetting properties are improved without the need for nanoparticle coating uniformity, which suggests ease of fabrication.

Figure 5 shows the micropillar/nanoparticle (Fig. 5(c)) and microcell/nanoparticle (Fig. 5(d)) surfaces. SEM images from the top (Figs. 5(c)(i) and 5(d)(i)) and 15° tilted view (Figs. 5(c)(ii) and 5(d)(ii)) are both shown. A zoomed-in SEM image is also shown for both structures. For 3D printed micropillars, adding a nanoparticle coating increased the water and oil contact angle from 156.7° ± 2.1° and 148.5° ± 2.0°, respectively, to 170.0° ± 1.5° (Fig. 5(a)(iv)) and 161.0° ± 2.5°, respectively. The water and ethylene glycol hysteresis values reduced from 30.0° ± 3.5° and 49.0° ± 5.5°, respectively, to 2.0° ± 1.5° and 4.5° ± 2.0°, respectively. The micropillars with nanoparticles structures have a measured breakthrough pressure of 1,130 ± 40 Pa (up from 1,020 ± 70 Pa prior to coating).

The microcells demonstrate similar improvement. The microcell water and ethylene glycol contact angle increased from 147.0° ± 2.0° and 138.0° ± 2.5°, respectively, to 167.3° ± 1.8° (Fig. 5(b)(iv)) and 159.5° ± 2.5°, respectively. The water and ethylene glycol hysteresis values reduced from 53.0° ± 4.5° and 64.3° ± 5.0°, respectively, to 2.5° ± 1.5° and 4.5° ± 2.0°, respectively, after nanoparticle coating. Microcells with nanoparticles structures have an experimental breakthrough pressure of 1,120 ± 40 Pa (up from 550 ± 70 Pa without nanoparticles). The static contact angle and contact angle hysteresis of the structures increased and decreased, respectively, due to smaller liquid–solid contact fractions, f_s. Furthermore, the breakthrough pressures also increase as the addition of the re-entrant nanospheres may provide for more metastable states where the droplet may pin. The integrated micro-/nanostructures demonstrate far better performance than the micro-/nanostructures alone indicating the importance of combining the 3D printed microstructures with nanoparticles in achieving high static contact angles and low contact angle hysteresis.

The structures were next tested for their abrasion durability. Figure 6 shows the results of abrasion durability tests for the micropillar/nanoparticles (Fig. 6(a)) and the microcell/nanoparticles (Fig. 6(b)). Figure 6(a)(i) shows how the static contact angle and contact angle hysteresis change with the abrasion cycle for micropillar array. After just a single cycle of abrasion, the water contact angle dropped significantly from 170.0° ± 1.5° to 91.0° ± 8.0°. The contact angle hysteresis also increased from an angle of 2.0° ± 1.5° to its maximum value of more than 90°, where the droplets stayed on the structure and did not roll off. The oil static contact angle also dropped from 161.0° ± 2.5° to 74.0° ± 12.0°. Figure 6(a)(ii) shows a SEM image of pillar array after one abrasion cycle. After just a single abrasion cycle, the majority of the micropillars, or approximately 70%, are destroyed. Since the maximum equivalent stress occurs at the base of the pillars, they are easily destroyed. As most of the micropillars are destroyed after a single abrasion cycle, the wetting properties do not change much after that, and almost all the pillars are completely destroyed after only 10 cycles of abrasion. These results

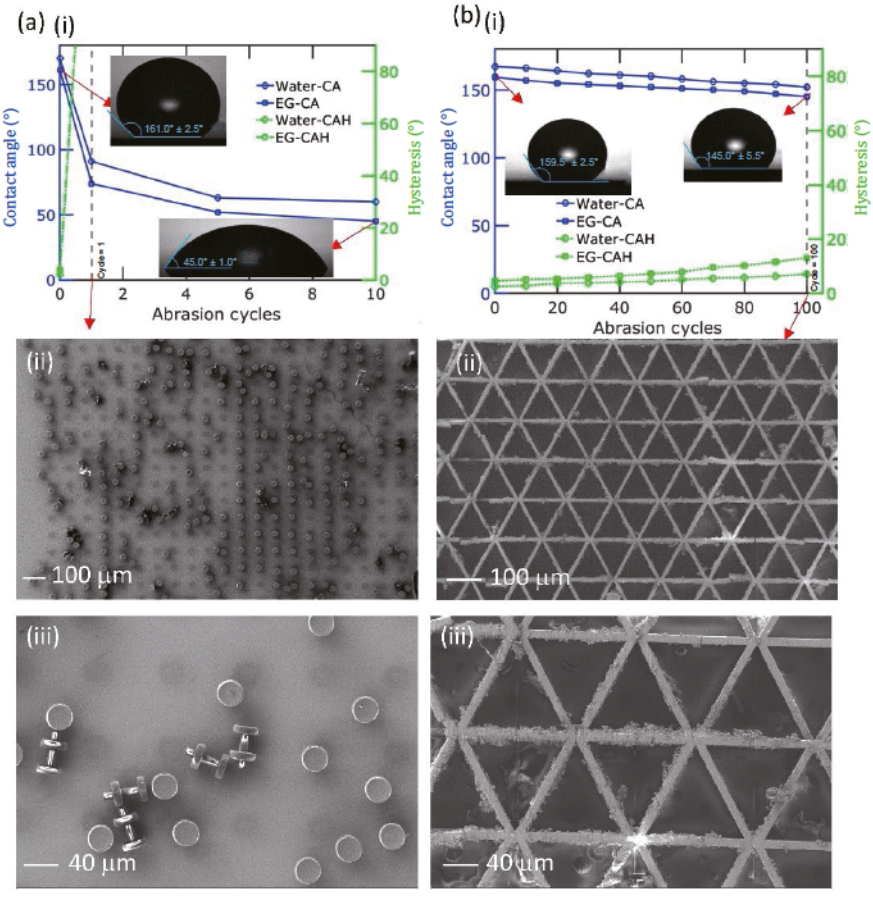

Figure 6 Water and ethylene glycol contact angle and hysteresis as a function of abrasion for (a)(i) micropillar/nanoparticles and (b)(i) microcell/nanoparticles. (a)(ii) and (iii) SEM images of micropillar/nanoparticles after 1 cycle of abrasion, in one direction only. Approximately 70% of pillars were destroyed. (b)(ii) and (iii) SEM images of microcell/nanoparticles after 100 cycles of abrasion.

suggest that micropillar arrays are not appropriate for real life applications.

In contrast, the microcell array shows much better mechanical durability. Figure 6(b)(i) shows the wetting behavior performance with abrasion of the microcell coated with nanoparticles. After 100 cycles of abrasion, the water contact angle was 152.0° ± 3.5° withhysteresisof7.1°±2.5°.Thecontactangleforethyleneglycoloilafter 100 cycles of abrasion was 145.0° ± 5.5° with hysteresis of 13.0° ± 6.5°. The microcell array remains superhydrophobic and has very high oil contact angle even after 100 cycles of harsh abrasion. Figure 6(b)(ii) shows the SEM image of the abraded sample after 100 cycles. The microcell array retains its morphology, while there is some residue left from the Scotch-Brite abrasive pad.

4 Conclusions

We report on super-repellent re-entrant microcell/nanoparticle array with high static contact angle, low hysteresis, high breakthrough pressure, and high mechanical durability. The re-entrant microcell/nanoparticle structures show static contact angles of 167.3° ± 1.8° and 159.5° ± 2.5° and contact angle hysteresis values of 2.5° ± 1.5° and 4.5° ± 2.0° for water and ethylene glycol oil, respectively. Abrasion tests as well as mechanical properties simulation results demonstrate that the microcell has very good mechanical durability. The water and oil contact angles for microcell arrays after 100 cycles of abrasion by Scotch-Brite abrasive pad with 1.2 kPa of pressure were 152.0° ± 3.5° and 145.0° ± 5.5°, respectively, with hysteresis of 7.1° ± 2.5° and 13.0° ± 6.5°, respectively. On the other hand, micropillar arrays lose their liquid repellency performance after just a single abrasion cycle. While micropillars may achieve higher static contact angle and breakthrough pressure simultaneously compared with microcells, their protrusive geometry results in very poor mechanical abrasion durability, which is likely to preclude their use in many applications. Integration of the 3D printed microstructures and nanoparticles are key to achieving a combination of both high static contact angle and low contact angle hysteresis. The microcell may be useful for a wide range of applications in medical devices, electronic devices, optoelectronics and many more.

Notes

The authors declare no competing financial interest.

Acknowledgement

This work was supported in part by the National Science Foundation (No. ECCS 1552712).

References

[1] Haghanifar, S.; Lu, P.; Kayes, M. I.; Tan, S. S.; Kim, K. J.; Gao, T.; Ohodnicki, P.; Leu, P. W. Self-cleaning, high transmission, near unity haze OTS/silica nanostructured glass. *J. Mater. Chem. C.* **2018**, *6*, 9191–9199.

[2] Nanda, D.; Varshney, P.; Satapathy, M.; Mohapatra, S. S.; Kumar, A. Self-assembled monolayer of functionalized silica microparticles for self-cleaning applications. *Colloids Surf. Physicochem. Eng. Asp.* **2017**, *529*, 231–238.

[3] Mahadik, S. A.; Kavale, M. S.; Mukherjee, S. K.; Rao, A. V. Transparent superhydrophobic silica coatings on glass by sol-gel method. *Appl. Surf. Sci.* **2010**, *257*, 333–339.

[4] Haghanifar, S.; McCourt, M.; Cheng, B. L.; Wuenschell, J.; Ohodnicki, P.; Leu, P. W. Creating glasswing butterfly-inspired durable antifogging superomniphobic supertransmissive, superclear nanostructured glass through Bayesian learning and optimization. *Mater. Horiz.* **2019**, *6*, 1632–1642.

[5] Wilke, K. L.; Preston, D. J.; Lu, Z. M.; Wang, E. N. Toward condensation-resistant omniphobic surfaces. *ACS Nano* **2018**, *12*, 11013–11021.

[6] Mouterde, T.; Lehoucq, G.; Xavier, S.; Checco, A.; Black, C. T.; Rahman, A.; Midavaine, T.; Clanet, C.; Quéré, D. Antifogging abilities of model nanotextures. *Nat. Mater.* **2017**, *16*, 658–663.

[7] Haghanifar, S.; Tomasovic, L. M.; Galante, A. J.; Pekker, D.; Leu, P. W. Stain-resistant, superomniphobic flexible optical plastics based on nano-enoki mushrooms. *J. Mater. Chem. A* **2019**, *7*, 15698–15706.

[8] Wang, N.; Xiong, D. S.; Pan, S.; Wang, K.; Shi, Y.; Deng, Y. L. Robust superhydrophobic coating and the anti-icing properties of its lubricants-infused-composite surface under condensing condition. *New J. Chem.* **2017**, *41*, 1846–1853.

[9] Meuler, A. J.; McKinley, G. H.; Cohen, R. E. Exploiting topographical texture to impart icephobicity. *ACS Nano* **2010**, *4*, 7048–7052.

[10] Kayes, M. I.; Galante, A. J.; Stella, N. A.; Haghanifar, S.; Shanks, R. M. Q.; Leu, P. W. Stable lotus leaf-inspired hierarchical, fluorinated polypropylene surfaces for reduced bacterial adhesion. *React. Funct. Polym.* **2018**, *128*, 40–46.

[11] Galante, A. J.; Haghanifar, S.; Romanowski, E. G.; Shanks, R. M. Q.; Leu, P. W. Superhemophobic and antivirofouling coating for mechanically durable and wash-stable medical textiles. *ACS Appl. Mater. Interfaces* **2020**, *12*, 22120–22128.

[12] Haghanifar, S.; Galante, A. J.; Leu, P. W. Challenges and prospects of bio-inspired and multifunctional transparent substrates and barrier layers for optoelectronics. *ACS Nano* **2020**, *14*, 16241–16265.

[13] Ragesh, P.; Ganesh, V. A.; Nair, S. V.; Nair, A. S. A review on 'self-cleaning and multifunctional materials'. *J. Mater. Chem. A* **2014**, *2*, 14773–14797.

[14] Pan, S. J.; Kota, A. K.; Mabry, J. M.; Tuteja, A. Superomniphobic surfaces for effective chemical shielding. *J. Am. Chem. Soc.* **2013**, *135*, 578–581.

[15] Choi, W.; Tuteja, A.; Chhatre, S.; Mabry, J. M.; Cohen, R. E.; McKinley, G. H. Fabrics with tunable oleophobicity. *Adv. Mater.* **2009**, *21*, 2190–2195.

[16] Ahuja, A.; Taylor, J. A.; Lifton, V.; Sidorenko, A. A.; Salamon, T. R.; Lobaton, E. J.; Kolodner, P.; Krupenkin, T. N. Nanonails: A simple geometrical approach to electrically tunable superlyophobic surfaces. *Langmuir* **2008**, *24*, 9–14.

[17] Kota, A. K.; Li, Y. X.; Mabry, J. M.; Tuteja, A. Hierarchically structured superoleophobic surfaces with ultralow contact angle hysteresis. *Adv. Mater.* **2012**, *24*, 5838–5843.

[18] Tuteja, A.; Choi, W.; Ma, M. L.; Mabry, J. M.; Mazzella, S. A.; Rutledge, G. C.; McKinley, G. H.; Cohen, R. E. Designing superoleophobic surfaces. *Science* **2007**, *318*, 1618–1622.

[19] Cassie, A. B. D.; Baxter, S. Wettability of porous surfaces. *Trans. Faraday Soc.* **1944**, *40*, 546–551.

[20] Marmur, A. From hygrophilic to superhygrophobic: Theoretical conditions for making high-contact-angle surfaces from low-contact-angle materials. *Langmuir* **2008**, *24*, 7573–7579.

[21] Chu, Z. L.; Seeger, S. Superamphiphobic surfaces. *Chem. Soc. Rev.* **2014**, *43*, 2784–2798.

[22] Sahoo, B.; Yoon, K.; Seo, J.; Lee, T. Chemical and physical pathways for fabricating flexible superamphiphobic surfaces with high transparency. *Coatings* **2018**, *8*, 47.

[23] Im, Y.; Joshi, Y.; Dietz, C.; Lee, S. S. Enhanced boiling of a dielectric liquid on copper nanowire surfaces. *Int. J. Micro-Nano Scale Transp.* **2010**, *1*, 79–96.

[24] Choi, J.; Jo, W.; Lee, S. Y.; Jung, Y. S.; Kim, S. H.; Kim, H. T. Flexible and robust superomniphobic surfaces created by localized photofluidization of azopolymer pillars. *ACS Nano* **2017**, *11*, 7821–7828.

[25] Liu, X. J.; Gu, H. C.; Wang, M.; Du, X.; Gao, B. B.; Elbaz, A.; Sun, L. D.; Liao, J. L.; Xiao, P. F.; Gu, Z. Z. 3D printing of bioinspired liquid superrepellent structures. *Adv. Mater.* **2018**, *30*, 1800103.

[26] Yang, Y.; Li, X. J.; Zheng, X.; Chen, Z. Y.; Zhou, Q. F.; Chen, Y. 3D-printed biomimetic super-hydrophobic structure for microdroplet

manipulation and oil/water separation. *Adv. Mater.* **2018**, *30*, 1704912.
[27] Hu, S. T.; Cao, X. B.; Reddyhoff, T.; Puhan, D.; Vladescu, S. C.; Wang, Q.; Shi, X.; Peng, Z. K.; deMello, A. J.; Dini, D. Self-compensating liquid repellent surfaces with stratified morphology. *ACS Appl Mater Interfaces* **2020**, *12*, 4147–4182.
[28] Liu, X. J.; Gu, H. C.; Ding, H. B.; Du, X.; He, Z. Z.; Sun, L. D.; Liao, J. L.; Xiao, P. F.; Gu, Z. Z. Programmable liquid adhesion on bio-inspired re-entrant structures. *Small* **2019**, *15*, e1902360.
[29] Mooraj, S.; Qi, Z.; Zhu, C.; Ren, J.; Peng, S. Y.; Liu, L.; Zhang, S. B.; Feng, S.; Kong, F. Y.; Liu, Y. F. et al. 3D printing of metal-based materials for renewable energy applications. *Nano Res.* **2021**, *14*, 2105–2132.
[30] Yoo, J. I.; Kim, S. H.; Ko, H. C. Stick-and-play system based on interfacial adhesion control enhanced by micro/nanostructures. *Nano Res.* **2021**, *14*, 3143–3158.
[31] Feng, L.; Zhang, Y.; Xi, J.; Zhu, Y.; Wang, N.; Xia, F.; Jiang, L. Petal effect: A superhydrophobic state with high adhesive force. *Langmuir* **2008**, *24*, 4114–4119.
[32] Chakraborty, M.; Weibel, J. A.; Schaber, J. A.; Garimella, S. V. The wetting state of water on a rose petal. *Adv. Mater. Interfaces* **2019**, *6*, 1900652.
[33] Zhou, Z. Y.; Gao, T. C.; McCarthy, S.; Kozbial, A.; Tan, S. S.; Pekker, D.; Li, L.; Leu, P. W. Parahydrophobicity and stick-slip wetting dynamics of vertically aligned carbon nanotube forests. *Carbon* **2019**, *152*, 474–481.
[34] Szczepanski, C. R.; Guittard, F.; Darmanin, T. Recent advances in the study and design of parahydrophobic surfaces: From natural examples to synthetic approaches. *Adv. Colloid Interface Sci.* **2017**, *241*, 37–61.
[35] Darmanin, T.; Guittard, F. Superhydrophobic and superoleophobic properties in nature. *Mater. Today* **2015**, *18*, 273–285.
[36] Barthlott, W.; Neinhuis, C. Purity of the sacred lotus, or escape from contamination in biological surfaces. *Planta* **1997**, *202*, 1–8.
[37] Milionis, A.; Loth, E.; Bayer, I. S. Recent advances in the mechanical durability of superhydrophobic materials. *Adv. Colloid Interface Sci.* **2016**, *229*, 57–79.
[38] Tian, X. L.; Verho, T.; Ras, R. H. A. Moving superhydrophobic surfaces toward real-world applications. *Science* **2016**, *352*, 142–143.
[39] Wang, D. H.; Sun, Q. Q.; Hokkanen, M. J.; Zhang, C. L.; Lin, F. Y.; Liu, Q.; Zhu, S. P.; Zhou, T. F.; Chang, Q.; He, B. et al. Design of robust superhydrophobic surfaces. *Nature* **2020**, *582*, 55–59.
[40] Zhao, R.; Chen, Y.; Liu, G. Z.; Jiang, Y. C.; Chen, K. L. Fabrication of self-healing waterbased superhydrophobic coatings from POSS modified silica nanoparticles. *Mater. Lett.* **2018**, *229*, 281–285.
[41] Wang, H. X.; Fang, J.; Cheng, T.; Ding, J.; Qu, L. T.; Dai, L. M.; Wang, X. G.; Lin, T. One-step coating of fluoro-containing silica nanoparticles for universal generation of surface superhydrophobicity. *Chem. Commun.* **2008**, *7*, 877–879.
[42] Brakke, K. A. The surface evolver. *Exp. Math.* **1992**, *1*, 141–165.
[43] Frenzel, T.; Kadic, M.; Wegener, M. Three-dimensional mechanical metamaterials with a twist. *Science* **2017**, *358*, 1072–1074.
[44] 3M United States. Scotch-Brite™ Aircraft Cleaning Pad[EB/OL]. https://www.3m.com/3M/en_US/p/d/b40066280/ (Accessed Dec 12, 2021).
[45] Leo, T. L.; Kim, C. J. C. J. Turning a surface superrepellent even to completely wetting liquids. *Science* **2014**, *346*, 1096–1100.
[46] Haghanifar, S.; McCourt, M.; Cheng, B. L.; Wuenschell, J.; Ohodnicki, P.; Leu, P. W.; Leu P. W.; Leu P. W. Discovering high-performance broadband and broad angle antireflection surfaces by machine learning. *Optica* **2020**, *7*, 784–789.
[47] Haghanifar, S.; Rodriguez De Vecchis, R. T.; Kim, K. J.; Wuenschell, J.; Sharma, S. P.; Lu, P.; Ohodnicki, P.; Leu, P. W. Flexible nanograss with highest combination of transparency and haze for optoelectronic plastic substrates. *Nanotechnology* **2018**, *29*, 42LT01.
[48] Haghanifar, S.; Gao, T. C.; Vecchis, R. T. R. D.; Pafchek, B.; Jacobs, T. D. B.; Leu, P. W. Ultrahigh-transparency, ultrahigh-haze nanograss glass with fluid-induced switchable haze. *Optica* **2017**, *4*, 1522–1525.
[49] Peng, K. Q.; Wang, X.; Li, L.; Wu, X. L.; Lee, S. T. High-performance silicon nanohole solar cells. *J. Am. Chem. Soc.* **2010**, *132*, 6872–6873.
[50] Panter, J. R.; Gizaw, Y.; Kusumaatmaja, H. Multifaceted design optimization for superomniphobic surfaces. *Sci. Adv.* **2019**, *5*, eaav7328.
[51] Wang, B. M.; Gao, T. C.; Zhou, Z. Y.; Pafchek, B.; Leu, P. W. Frontside scattering structures for enhanced performance in flexible ultrathin crystalline silicon solar cells. *J. Photon. Energy* **2018**, *8*, 030501.
[52] Gao, T. C.; Haghanifar, S.; Lindsay, M. G.; Lu, P.; Kayes, M. I.; Pafchek, B. D.; Zhou, Z. Y.; Ohodnicki, P. R.; Leu, P. W. Fundamental performance limits and haze evaluation of metal nanomesh transparent conductors. *Adv. Opt. Mater.* **2018**, *6*, 1700829.